

# Dwarf Galaxies in Voids: Dark Matter Halos and Gas Cooling

Matthias Hoeft<sup>1</sup> & Stefan Gottlöber<sup>2</sup>

<sup>1</sup>Thüringer Landessternwarte Tautenburg, 07778 Tautenburg, Germany

<sup>2</sup>Astrophysikalisches Institut Potsdam, 14482 Potsdam, Germany

October 19, 2018

## Abstract

Galaxy surveys have shown that luminous galaxies are mainly distributed in large filaments and galaxy clusters. The remaining large volumes are virtually devoid of luminous galaxies. This is in concordance with the formation of the large-scale structure in Universe as derived from cosmological simulations. However, the numerical results indicate that cosmological voids are abundantly populated with dark matter haloes which may in principle host dwarf galaxies. Observational efforts have in contrast revealed, that voids are apparently devoid of dwarf galaxies. We investigate the formation of dwarf galaxies in voids by hydrodynamical cosmological simulations. Due to the cosmic ultra-violet background radiation low-mass haloes show generally are reduced baryon fraction. We determine the characteristic mass below which dwarf galaxies are baryon deficient. We show that the circular velocity below which the accretion of baryons is suppressed is approximately  $40 \text{ km s}^{-1}$ . The suppressed baryon accretion is caused by the photo-heating due to the UV-background. We set up a spherical halo model and show that the effective equation of state of the gas in the periphery of dwarf galaxies determines the characteristic mass. This implies that any process which heats the gas around dwarf galaxies increases the characteristic mass and thus reduces the number of observable dwarf galaxies.

*send offprint requests to: hoeft@tls-tautenburg.de*

## 1 Introduction: Formation of Structure in the Universe

During the last couple of decades new extensive observations of the Universe were made using both ground-based telescopes and space instruments. These measurements have provided new insights into the structure of the Universe on various scales. A wide range of the electromagnetic spectrum emitted by cosmic objects has been studied. The wavelengths extend from very long radio wavelengths to energetic gamma rays. This observational progress has been accompanied by considerable effort in our theoretical understanding of the formation of different components of the observed structure of the Universe from small scales (galaxies and their satellites) up to the largest scales (clusters of galaxies and superclusters).

The standard picture of structure formation was suggested by White and Rees [70] more than 30 years ago. It suggests that gravitational instability drives the dark matter (DM) to cluster hierarchically in a bottom-up fashion. The gaseous baryons settle into the DM haloes (namely, bound virial DM structures) and via gas-dynamical dissipative processes cool, fragment and form stars. This simple picture prevails today, although our knowledge of the details and of the actual processes has evolved dramatically since then. The non-linear nature of the gravitational dynamics and the gas-astrophysical processes makes the problem of structure formation virtually

intractable analytically, and therefore the field relies on numerical simulations. A substantial part of the progress in understanding structure formation in the universe is due to the increasing possibilities to make numerical experiments using the largest massive parallel supercomputers. In the eighties the best simulations handled  $32^3$  particles whereas at present  $1024^3$  particles became a standard for numerical simulations, a increase of  $2^{15}$  roughly in agreement with Moore's law.

The effort of observers and theorists brought about the so called standard cosmological model. This model is based on the idea that some kind of dark energy contributes about 70% of the total energy density of the spatially flat Universe in which the total energy density equals the critical one. The dark energy is responsible for the observed accelerated expansion of the universe. The simplest form of the dark energy is the cosmological constant, which was introduced already in 1917 by Albert Einstein in his paper about the cosmological solutions of the field equations of general relativity. The remaining about 30% of energy density consists of matter. About 85% of this matter is made of unknown dark matter particles, the remaining 15% is the contribution of "normal" baryonic particles well known to particle physicists. This means that the nature of more than 95% of the matter in the Universe is not yet understood.

According to this standard cosmological model, the main process responsible for the formation of the observed structures is gravitational instability. The initial seeds, which eventually became galaxies and superclusters and all other structures, came from the quantum fluctuations generated during the early inflationary phase:  $\sim 10^{-35}$  sec or so from the beginning of the Big Bang. The power spectrum of these primordial fluctuations has been confirmed by measuring the temperature fluctuations of the cosmic microwave background radiation. These temperature fluctuations tell us the magnitude of the small fluctuations in the Universe about 300 000 years after the Big Bang.

One of the key features of the standard model is its simplicity. The expansion rate and the clustering properties are described by only few parameters which are measured at present with quite high accuracy. These parameters are the current rate of universal expansion,  $H_0 = h \times 100 \text{ km s}^{-1} \text{ Mpc}^{-1}$ , the mass density parameter,  $\Omega_{\text{mat}}$ , the value of the cosmological constant,  $\Omega_{\Lambda}$ , the primordial baryon abundance,  $\Omega_{\text{b}}$ , and the overall normalisation of the power spectrum of initial density fluctuations, typically characterised by  $\sigma_8$ , the present-day r.m.s. mass fluctuations on spheres of radius  $8 h^{-1} \text{ Mpc}$ .

The initial power spectrum (created during the inflationary phase) does not contain preferred length scales. However, the horizon size at matter-radiation equality is mapped on this scale free spectrum. Since this scale (today around 100 Mpc) is well above the typical scales of observed objects structure formation is predicted to be essentially scale invariant: in a statistical sense the structures on scales of galaxy clusters are repeated on scales of galaxies. Typically, small objects merge together and form more and more massive objects. However, the small objects do not disappear within those larger objects but rather form a complex hierarchy of substructures. This hierarchical scenario predicts that our Milky Way galaxy is expected to have as many satellites (many hundreds) as a cluster of galaxies has galaxies. However, only a few dozen satellite of the Milky Way have been observed yet: this is the well known missing satellite problem [33, 43]. Other manifestations of the scale free power spectrum are the predicted large number of dwarfs in low density regions of the universe [17, 49] or the predicted spectrum of mini-voids in the Local Universe [62].

A better understanding of the physics of structure formation on small scales, in particular of the correct modelling of baryonic physics, could solve these problems [22]. Based on semi-analytical models recently Maccio *et al.* [40] (see also Ref. [34]) claimed that the long standing problem of missing satellites can be solved within the  $\Lambda$ CDM scenario. The basic idea behind this solution of the problem is that the haloes which host a galaxy of a given

measured rotational velocity are more massive than expected by the direct association of rotational velocity and the haloes maximum circular velocity. Since more massive haloes are less frequent the problem of missing satellites is solved. However, any non-baryonic physics that reduces power on small scales compared to the standard model will also improve the situation. It is well known that warm dark matter acts in this direction by erasing power at short scales due to free streaming [61, 72].

Altogether, we arrive at a picture in which dark matter particles form the backbone structure for all objects in the Universe from clusters of galaxies to dwarf galaxies. Normal matter (baryons) falls into the potential wells formed by the dark matter particles and forms the luminous objects. The details of this formation process must be followed using hydrodynamical simulations. Galaxy formation depends on many physical processes, some of which are very poorly understood, and some of which take place on sub-grid scales and therefore cannot be modelled fully and consistently and need to be fudged numerically by ad-hoc recipes. For example the formation of stars and the feedback of stars on the intergalactic medium take place on scales orders of magnitudes below the present day resolution. In cosmological simulations of galaxy formation typical masses of “stellar particles” are  $10^4 h^{-1} M_{\odot}$  or more. Thus such a particle represents the formation and evolution of a large number of real stars.

The paper is organised as follows: In Sec 2 we introduce briefly the method of cosmological simulations and discuss observational facts about voids and how they are defined in simulations. In Sec. 3 we present the baryon fraction in low mass dark matter haloes and introduce the characteristic mass. In Sec. 4 we introduce a spherical model for the halo gas and discuss the relation between photo-heating of the halo gas and gas accretion. Our findings are summarised in Sec. 5.

## 2 Cosmological simulations

The cosmic microwave background (CMB) originates from the recombination of the hydrogen in the Universe at redshift about 1000. Primordial small density fluctuations are imprinted on the spectrum of the CMB temperature fluctuations which is closely related to the initial power spectrum of density fluctuations. The observed unique features of CMB temperature fluctuations constrain the cosmological parameters as well as the normalisation of the power spectrum of density fluctuations. The most recent results of the WMAP experiment combined with the measurements of the baryonic oscillations and supernova data [21] yield a Hubble parameter  $h = 7.01$ , the density of dark matter  $\Omega_{\text{DM}} = 0.228$ , the baryonic density  $\Omega_{\text{bar}} = 0.046$ , the cosmological constant  $\Omega_{\Lambda} = 0.726$ , the normalisation of the power spectrum  $\sigma_8 = 0.82$  and its slope  $n = 0.96$ . These parameters fix the cosmological model and therefore also the power spectrum of the initial perturbations. Starting with the initial conditions the simulations follow the growth of the perturbation in a universe that expands according to the chosen cosmological parameters. In this expanding universe the gravitational interaction is Newtonian.

### 2.1 Initial conditions

The first step of running cosmological simulations is to set up the initial conditions, namely amplitudes and phases of small perturbations at a very high redshift. Having in mind that the largest structures in the universe – superclusters and voids – have sizes of 10 to 50 Mpc, the simulated volume should be significantly larger. However, we may be interested in the structure of a much smaller object such as our Milky Way galaxy or its satellites. In  $N$ -body simulations each mass element is represented by a point-like particle. The mass resolution is limited by the total number of particles computers can handle at a given time. Thus, increasing the representative cosmological volume decreases the mass resolution. To overcome this problem mass refinement techniques have been developed. Here we follow the algorithm proposed in Ref. [32]: To construct

suitable initial conditions, we first create a random realisation at the highest possible resolution. This depends on the available computers; at present we reach  $4096^3$  particles. The initial displacements and velocities of  $N$  particles are calculated using all waves ranging from the fundamental mode  $k = 2\pi/L_{\text{box}}$  to the Nyquist frequency  $k_{\text{Ny}} = 2\pi/L_{\text{box}} \times N^{1/3}/2$ . Then the resolution can be decreased by replacing  $8^i$  ( $i = 1, 5$ ) neighbouring particles by one particle with  $8^i$  higher mass which results in a distribution of  $2048^3$ ,  $1024^3$ ,  $512^3$ ,  $256^3$  or  $128^3$  particles. Using a smaller number of more massive particles we first run low-resolution simulations until the present epoch. In this simulation we select the regions of interest. Then we repeat the simulation but this time we preserve low mass particles inside the region of interest. Outside of this region we progressively replace small particles by massive ones creating shells of more and more massive particles until we reach the low resolution region of  $128^3$  particles. This procedure ensures that our object evolves in the proper cosmological environment and with the right gravitational tidal fields.

Based on the power spectrum of density fluctuations we set up the initial conditions of our simulation at an early redshift which depends on the size of the box and the required resolution. To move the particles from the original Lagrangian point on a regular grid to their Eulerian position we use the Zeldovich approximation. The power spectrum of the generated Gaussian stochastic density field corresponds to the input power spectrum. The random nature of the realisation manifests itself on scales comparable to the box size where the spectrum is sampled only by a few modes. By this procedure the cosmological parameters and the normalisation of the density power spectrum fully determine the initial conditions of the cosmological simulations, except of a random number which characterises the starting point of the random number generator. Thus, on scales comparable to the box size cosmic variance enters through this number which characterises a given simulation. On smaller scales - typically a quarter of the box size - the realisation follows very closely the input power spectrum. Starting from the initial matter distribution we sim-

ulate the formation of cosmological structures. More precisely, we integrate the Poisson equation by the help of particle methods (Gadget and ART).

## 2.2 The simulation method

Our hydrodynamical simulations have been run with an updated version of the parallel Tree-SPH code Gadget [58, 60]. The dark and baryonic matter distributions are represented by particles. The gravitational forces are computed by a new algorithm based on the Tree-PM method which speeds up the force computation significantly compared with a pure tree algorithm. The hydrodynamical equations are solved by a Smoothed-Particle Hydrodynamics (SPH) method. The code uses an entropy-conserving formulation of SPH [58] which alleviates problems due to numerical over-cooling.

The code also includes photo-ionisation and radiative cooling processes for an optically thin primordial mix of helium and hydrogen. For computing the thermal evolution it uses ionisation, recombination and cooling rates as given in Ref. [29]. Since we will set up later in this paper an analytic model for the evolution of the intergalactic medium (IGM) we give here in detail the processes which affect the temperature,  $T$ , of the IGM. It primarily changes due to photo-heating,  $\mathcal{H}$ , and radiative cooling,  $\Gamma$ . Moreover, it decreases due to the adiabatic Hubble expansion,  $dT \propto H dt$ , where  $H$  is the time-dependent Hubble constant. Cosmological structure formation changes the temperature adiabatically,  $dT \propto d\rho$ . Finally, changes of the chemical composition also affect the temperature,  $dT \propto d\Sigma_i X_i$ , where  $X_i$  denotes the abundance of the atomic species  $i$  with respect to the cosmic baryon density,  $X_i = n_i/n_b$ . In summary, the temperature evolution is given by

$$dT = \frac{2(\mathcal{H} - \Gamma) dt}{3 k_B n_b \Sigma_i X_i} - 2HT dt + \frac{2T d\Delta}{3 \Delta} - \frac{T d(\Sigma_i X_i)}{\Sigma_i X_i}, \quad (1)$$

where  $\Delta$  denotes the overdensity,  $\Delta = \rho/\langle\rho\rangle$ . We take the atomic hydrogen and helium species, {HI,

HII, HeI, HeII, HeIII}, into account. We assume a constant, primordial helium mass fraction of  $Y_p = 0.24$ .

The physics of star formation is treated in the code by means of a sub-resolution model in which the gas of the interstellar medium (ISM) is described as a multiphase medium of hot and cold gas [59,71]. Cold gas clouds are generated due to cooling and they are the material out of which stars can be formed in regions that are sufficiently dense. Supernova feedback heats the hot phase of the ISM and evaporates cold clouds, thereby establishing a self-regulation cycle for star formation. The heat input due to the supernovae also leads to a net pressurisation of the ISM, such that its effective equation of state becomes stiffer than isothermal. This stabilises the dense star forming gas in galaxies against further gravitational collapse, and allows converged numerical results for star formation even at moderate resolution. See [59] for a more detailed description of the star formation model implemented in the Gadget code.

### 2.3 Dark matter haloes

During the cosmological evolution dark matter haloes are formed which accrete more and more matter or merge with other ones. Within a simulation with one billion particles it is a challenge to find structures and substructures. To find structures at virial over-density one can use a friends-of-friends algorithm with a certain linking length (0.17 of the mean inter-particle distance for the  $\Lambda$ CDM model at redshift zero). The resulting particle clusters are in general tri-axial objects. Substructures can be identified as particle clusters at smaller linking lengths (higher over-densities). The more different linking lengths are used the better substructures will be resolved. Thus a whole hierarchy of friends-of-friends clusters have to be calculated. To this end we have developed a hierarchical friends-of-friends algorithm which is based on the calculation of the minimum spanning tree of the given particle distribution. We use also the bound-density-maxima (BDM) algorithm [31] which determines spherical haloes and their sub-haloes. The code removes

unbound particles which is particularly important for sub-haloes.

At all redshifts the sample of haloes is characterised by the mass function of the isolated haloes. This number density of haloes of a given mass depends on the power spectrum. A first very successful analytical ansatz to predict the mass function of haloes has been made by Press and Schechter [52]. Later on this has been improved by Bond *et al.* [2] and Sheth and Tormen [56]. The search for an accurate and universal function which describes the number density of haloes found in simulation at different redshifts led to a set of fitting functions proposed by different authors [27, 63, 68].

### 2.4 Voids

With the first available large galaxy surveys it became clear that there exist large regions in the Universe which are not occupied by bright galaxies [18, 28, 30]. Regions of all possible sizes devoid of galaxies can be seen in all redshift surveys. The observational discovery was soon followed by the theoretical understanding that voids constitute a natural outcome of structure formation via gravitational instability [23, 48]. Together with clusters, filaments, and superclusters, giant voids constitute the large-scale structure of the Universe.

More than 20 years ago, for the first time the sizes of voids have been estimated in different samples of galaxies with measured redshifts [7]. Later on voids in the CfA redshift catalogues were studied by [66], in the Las Campanas redshift survey by [44], in the Optical Redshift Survey and in the IRAS 1.2-Jy survey by [9, 10] and in the PSCz catalogue by Plionis and Basilakos [50] and Hoyle and Vogeley [25]. For a review of early observational efforts see Peebles [49]. More recently voids have been studied by many authors using the Two-Degree Field Galaxy Redshift Survey [4, 6, 26, 47] and the Sloan Digital Sky Survey [16, 24, 53, 67].

There were several attempts to find dwarf galaxies in few individual voids [19, 35, 38, 51]. The overall

conclusion is that faint galaxies do not show a strong tendency to fill up voids defined by bright galaxies. The strongest arguments that voids are not populated by dwarf galaxies were given by Peebles [49] who points out that the dwarf galaxies in the ORS catalogue follow remarkably close the distribution of bright galaxies: there are no indications that they fill voids in the distribution of bright galaxies. To summarise, observations indicate that large voids found in the distribution of bright ( $\sim M_*$ ) galaxies are empty of galaxies, which are two magnitudes below  $M_*$ . Recently, Tikhonov and Klypin [62] studied the properties of mini-voids in the nearby universe.

The void phenomenon was already the target of many theoretical studies [1, 8, 12–15, 36, 41, 54, 55]. Using a set of DM only simulations [17] have studied the inner structure of voids. The haloes in voids are arranged in a pattern, which looks like a miniature Universe with the same structural elements as the large-scale structure of the galactic distribution of the Universe. There are filaments and voids; larger haloes are at the intersections of filaments. The mass function of haloes in voids is much steeper for high masses resulting in very few galaxies with circular velocities  $v_{\text{circ}} \approx 100 \text{ km s}^{-1}$ . Note, however, that in DM simulations it has been usually assumed that each dark matter halo hosts at least one galaxy. This may not be true. Physical processes of galaxy formation are not well known and there could be processes that strongly suppress the formation of stars inside small haloes, which collapse relatively late in voids. This issue will be discussed in detail in the following sections.

There is a lot of interest in the void phenomena. However, there is no clear definition of a void. Almost every study uses its own definition of a void and its own void finder. Recently, the different approaches have been compared within the Aspen-Amsterdam Void Finder Comparison Project [5]. Here we use a rather simple and direct definition. In order to identify voids, we start with a selection of point like objects in 3D. These objects can be haloes above a certain mass or a certain circular

velocity or galaxies above a certain luminosity. Thus the voids are characterised by the threshold mass or luminosity. The void finding algorithm can be applied both to numerical and observational data. In numerical simulations it takes into account periodic boundary conditions. At first it searches the largest empty sphere which is completely inside the given volume. The radius of this empty region is  $R_{\text{void}}$ . Then we extend this region to an empty region with irregular shape. We define this empty region as union of all spheres with radius  $r_{\text{ext}} \geq 0.789 R_{\text{void}}$  (thus with a volume greater or equal half of the volume of the original void sphere) which can be moved to their place without crossing any object or the box boundary. To find the other voids we repeat this procedure however taking into account the previously found voids. We now search the largest empty sphere which is completely inside the volume and does not intersect with any already known void. The voids are characterised by volume, shape and orientation.

For the re-simulation we selected a void region from a larger periodic computational box. To construct suitable initial conditions, at first we replaced in a box of side-length  $50 h^{-1} \text{ Mpc}$  with  $2048^3$  particles the low mass particles by  $256^3$  massive ones. After running the simulation at this low mass resolution we determined a void region of interest and, finally, we were rerunning the simulation with the original set of particles inside the void ( $2048^3$ ) and replacing only outside the void the low mass particles by more massive ones.

### 3 The baryon content of dwarf galaxy haloes

The number density of dwarf galaxies observed in the Universe is apparently smaller than the predicted number density of low mass dark matter haloes [65]. The missing galaxies are either not formed because the corresponding dark matter haloes do not exist, or no stars are formed in small haloes. As shown by Hoefft et al. [22] and Okamoto et al. [46], the op-

refined region	simulation bos size	mass resolution (dark matter)
void	$50 h^{-1} \text{ Mpc}$	$1.03 \times 10^6 h^{-1} M_{\odot}$
filament	$80 h^{-1} \text{ Mpc}$	$8.24 \times 10^6 h^{-1} M_{\odot}$

**Table 1:** Main characteristics of the two simulations analysed for determining the characteristic mass.

tically thin UV-background already causes baryon deficiency in small haloes. In this section we determine the mass scale below which photo-heating causes baryon deficiency.

### 3.1 Mass accretion history

The gravitationally bound structures, i.e. galaxies and clusters of galaxies, grow in two ways: they accrete surrounding matter and they merge with other galaxies or clusters. Numerical simulations allow us to follow the merging history of the haloes. Every massive halo at the end of the simulation has a large number of progenitors which subsequently merge to the final structure.

We compute the mass accretion history for all haloes in our two simulations, see Tab. 1. To this end we determine the haloes in each simulation snapshot. Then we go backward from the final snapshot and search for the most massive progenitor in the previous snapshot. Since we have stored more than one hundred snapshots for each simulation we can simply search for the most massive progenitor in the vicinity of a given halo. However, during merger events the halo finder sometimes fails to identify the halo at all, since two approaching haloes appear spuriously gravitationally unbound. Fig. 1 shows the mass accretion histories of ten sample haloes, where the jumps are caused by merger events.

### 3.2 Characteristic mass

We determine for all distinct haloes in our simulations the baryon fraction within the virial radius,  $f_b = M_{\text{bar}}/M_{\text{tot}} = (M_{\text{star}} + M_{\text{gas}})/(M_{\text{star}} + M_{\text{gas}} + M_{\text{dm}})$ , where  $M_{\text{bar}}$  denotes the baryonic mass,  $M_{\text{tot}}$  the to-

tal mass,  $M_{\text{dm}}$  the dark matter mass,  $M_{\text{gas}}$  the gas mass and  $M_{\text{star}}$  in stellar mass. We take those haloes into account which consist of more than 180 dark matter particles. The resulting lowest halo mass is  $1.9 \times 10^8 h^{-1} M_{\odot}$  and  $1.5 \times 10^9 h^{-1} M_{\odot}$  for the void and for the filament region, respectively. Moreover, we exclude all haloes which have been within the virial radius of a more massive halo in the past, because the dark matter and baryonic masses may be affected by stripping. Fig. 2 shows the resulting baryon fraction for both the low density region simulation the filament region simulation. The low mass haloes evidently have a baryon fraction much smaller than the cosmic baryon fraction. Since the transition from ‘cosmic mean baryon fraction’ to ‘baryon deficient’ occurs within a rather small mass range this phenomenon can be characterised by a single parameter, namely the mass at which the baryon fraction amounts in average to half of the cosmic mean,  $M_{1/2}$ . We determine the characteristic mass computing the average baryon fraction in mass bins and approximating the resulting curve by the following analytic expression

$$f_b = \langle f_b \rangle \left\{ \frac{1}{2} + \frac{1}{\pi} \arctan \left( \frac{\log M_{\text{tot}} - \log M_{1/2}}{w_M} \right) \right\}. \quad (2)$$

We use a different expression than in Ref. [22] to make the fitting procedure more robust, in particular when a second free parameter is included, here the width  $w_M$ . Moreover, we expect that the halo gas, which is present independently from the halo size, leads to a floor in the baryon fraction. As we have shown in Ref. [22] the characteristic mass depends very little on the mass resolution used in our simulations. This indicates that the physical processes causing the baryon deficiency are reasonably resolved even if there are only a few tens of gas particles in small mass haloes.

In Ref. [22] we focussed on the baryon content of dwarf galaxies in cosmological voids. The result we obtained might be affected by restricting to void dwarf galaxies. To investigate also the effect

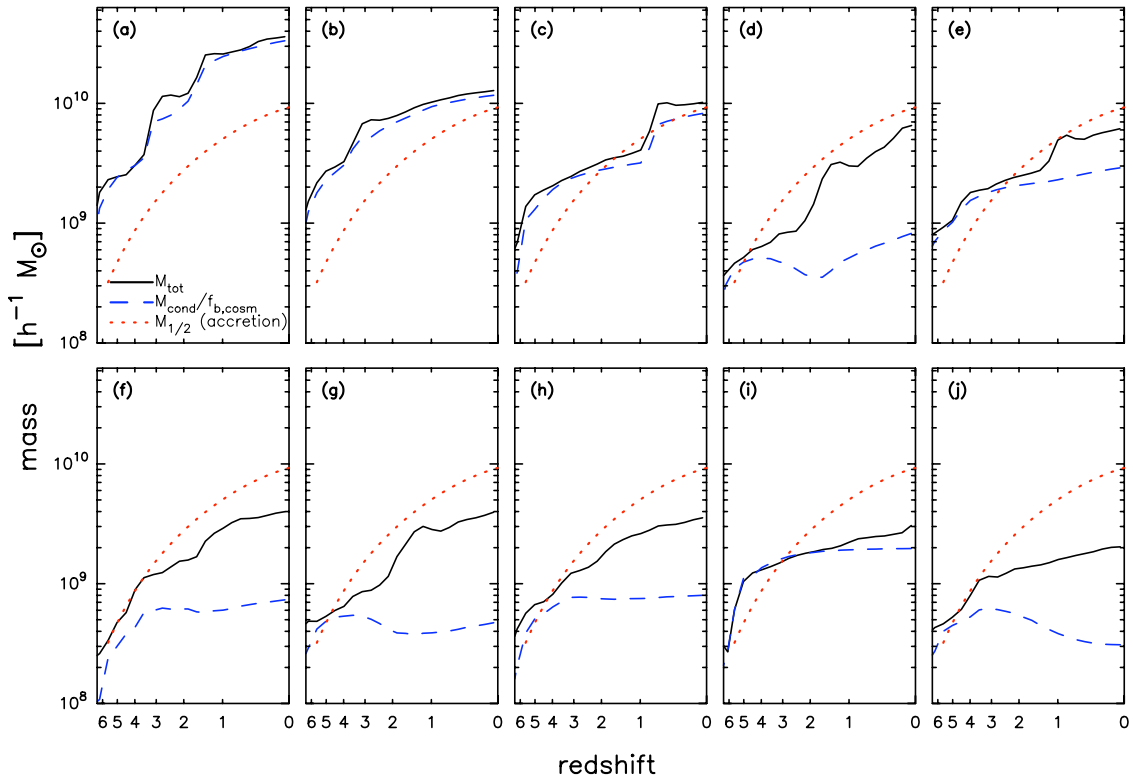


**Figure 1:** The mass accretion histories for several haloes. In each panel the total mass (solid line) and the condensed mass (dashed line) of one halo is shown. We have divided the condensed mass by the mean cosmic baryon fraction,  $\langle f_b \rangle$ , to highlight when the condensed mass does not follow the expectation according to the mean baryon density. In addition, the characteristic mass (dotted line) is shown as derived from baryon fraction in newly accreted matter. One can clearly see that haloes cease to condense baryons when their total mass falls below the characteristic mass.

of the cosmological environment we include here dwarf galaxies in a cosmological filament. These galaxies have a higher merger rate than void dwarf galaxies with a similar mass but they do accrete less diffuse gas, see Ref. [11] and references therein. We have excluded all galaxies which have passed through the halo of a more massive galaxy since their dark matter and baryonic mass could be affected by stripping. Despite the cosmologically quite different environments, the characteristic mass of both regions coincide well, see Fig. 2 (top row). In conclusion, the general mass accretion history of a dwarf galaxy has only little effect on their baryon content, i. e. there is universal characteristic

mass for all dwarf galaxies. Note, this result is obtained with a homogeneous UV-background. We will argue later that the UV-heating may have a crucial impact on the baryon accretion in dwarf galaxies.

Observationally, the total mass of a galaxy is difficult to determine. Galaxies are preferably characterised by the maximum circular velocity,  $v_{\max}$ . One should note that also  $v_{\max}$  is difficult to measure in dwarf galaxies since most rotation curves do not approach a maximum, i. e. the maximum of the circular velocity lies outside the observable gas distribution. However, we will characterise haloes mainly by  $v_{\max}$ . Fig. 2 (middle row) shows the



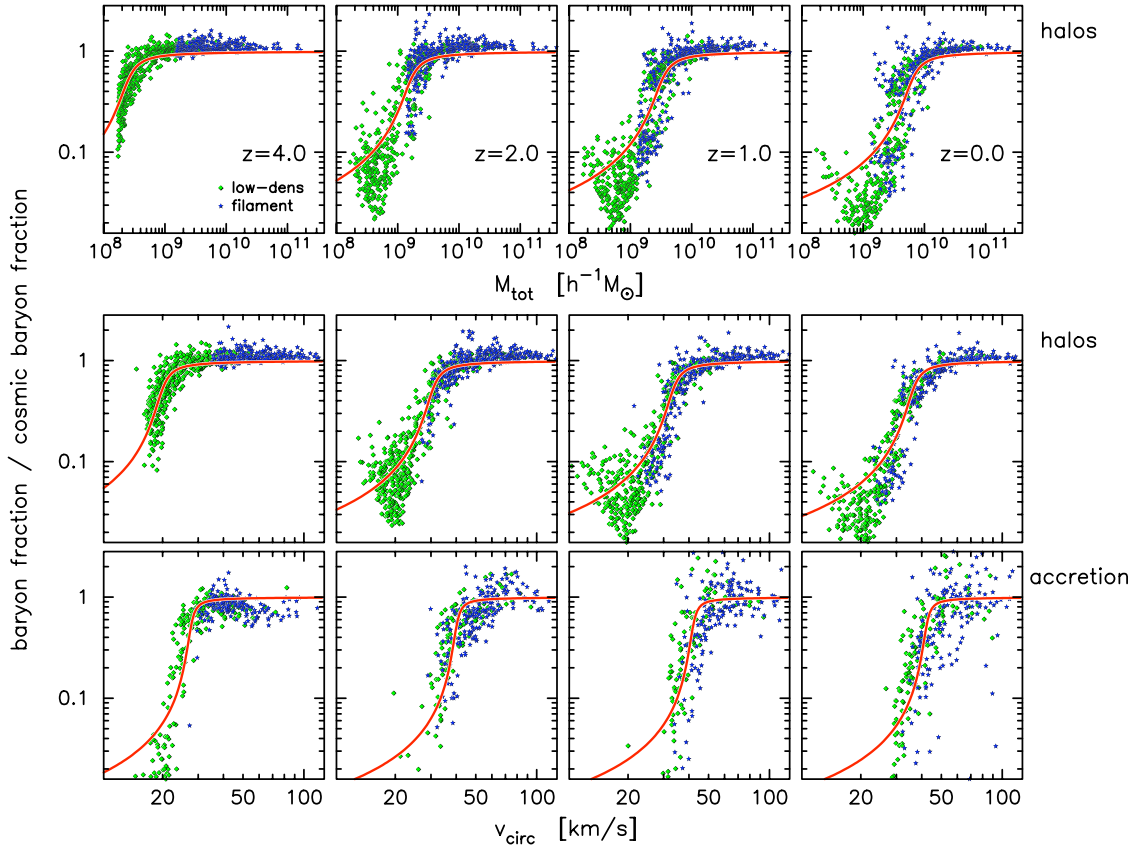


**Figure 2:** The baryonic mass fraction in units of the cosmic mean,  $\Omega_b/\Omega_m$ . Filled squares refer to the simulation of low density region while stars refer to the filament region. Only haloes with more than 180 dark matter are taken into account. The top row shows the baryon fraction at different redshifts as a function of total halo mass. The middle row gives the baryon fraction as a function of maximum circular velocity. The bottom row shows the baryon fraction of newly accreted matter (see text for a more detailed description).

baryon fractions in distinct haloes as a function of the maximum circular velocity.

Our aim is to determine what makes haloes below the characteristic mass baryon deficient. The baryon content at a given time is accumulated over the history of the halo. To assess what prevents at a given time haloes from accreting baryonic mass we determine the baryon fraction of newly accreted matter

$$f_b^{\text{accr}} = \frac{M_{\text{cond}}(t_{i+1}) - M_{\text{cond}}(t_{i-1})}{M_{\text{tot}}(t_{i+1}) - M_{\text{tot}}(t_{i-1})}, \quad (3)$$

where  $t_{i-1}$  and  $t_{i+1}$  denote the masses of a given halo at an earlier and at a later time, respectively. Fig. 2 (bottom row) shows that small haloes do not accrete baryonic mass. Since we consider the differential evolution of the dark matter and the baryonic masses we have a large scatter in the characteristic mass of newly accreted matter. However, similar to the baryon fraction in haloes there is a clear separation between low mass haloes which accrete virtually no baryonic matter and high mass haloes which accrete matter with the mean cosmic baryon fraction.

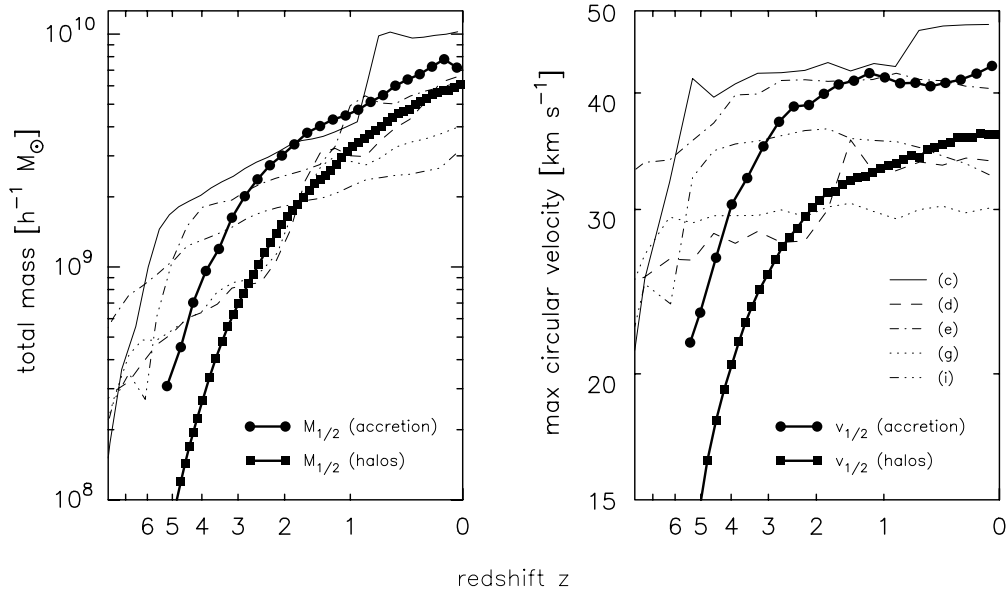


**Figure 3:** *Left panel:* Evolution of the characteristic mass of the baryon fraction in distinct haloes (squares) and in newly accreted matter (circles). For comparison the mass accretion histories of five haloes, as depicted in Fig. 1, are shown. *Right panel:* Evolution of the characteristic circular velocity in distinct haloes and in newly accreted matter. Additionally, the circular velocity histories of the haloes in the left panel is shown.

### 3.3 Evolution of the characteristic mass

Fig. 2 shows that the characteristic mass decreases with redshift. For instance, at redshift  $z = 4$  the characteristic mass is about  $3 \times 10^8 h^{-1} M_{\odot}$ , while it amounts to  $6 \times 10^9 h^{-1} M_{\odot}$  at  $z = 0$ . Fig. 3 shows the redshift evolution of the characteristic mass as obtained from combined halo lists from our two simulations. For comparison also a few mass accretion histories from Fig. 1 are shown.

Plotted as a function of circular velocity the evolution of the characteristic mass of the newly accreted matter has a rather simple behaviour: after a steep increase it is almost constant at  $\sim 40 \text{ km s}^{-1}$  for  $z \lesssim 3$ . Note, in Ref. [22] we found a lower value since we used the circular velocity at the virial radius,  $v(r_{\text{vir}})$ , instead of  $v_{\text{max}}$ . Moreover, we considered only the baryon fraction in haloes. Since semianalytic models of galaxy formation

assume a low-mass cut-off for gas accretion, see e.g. Ref. [57] and Ref. [37], we investigate here also the characteristic mass of newly accreted matter.

Because the circular velocity of most of the dwarf galaxy haloes is almost constant with time, except a major merger occurs, one can separate two types of evolutionary scenarios for dwarf galaxies: (i) small galaxies with  $v_{\text{max}} \ll 40 \text{ km s}^{-1}$  accrete baryons only for  $z \gtrsim 4$  and (ii) galaxies with  $v_{\text{max}} \gg 40 \text{ km s}^{-1}$  are not affected at all. In Fig. 1 we have also depicted for each halo the evolution of  $M_{1/2}^{\text{accr}}$  as shown in Fig. 3 (left panel). One can see nicely that haloes get baryon deficient when their halo mass is below  $M_{1/2}^{\text{accr}}$ .

### 3.4 Can the characteristic mass explain the void phenomenon?

The void phenomenon comprises two observational findings [49]: First, the distribution of massive galaxies ( $\geq L_*$ ) shows large empty regions, the ‘voids’, see

Sec. 2.4. Low-luminosity galaxies populate the voids but with a low volume density compared to the dense regions [24]. Secondly, the galaxies found in voids are not special at all. According to the concordance  $\Lambda$ CDM cosmology voids are filled by dark matter haloes with the size of dwarf galaxies [17]. To judge if this is at odds with the void phenomenon in observations one has to assign a luminosity to the dark matter haloes. Recently, Tinker and Conroy [64] applied a Halo Occupations Distribution (HOD) to a large dark matter simulation and analysed void regions. They found that the haloes in void regions which host galaxies with an absolute magnitude  $M_r > -10$  are located close to the walls of the voids. Only even fainter galaxies, i.e. galaxies which are significantly below the current detection limit of surveys covering large void regions [24], populate the entire void volume. According to Tinker and Conroy galaxies with  $M_r = -10$  reside in haloes with a mass  $\sim 10^{10} h^{-1} M_\odot$ . Hence, the photo-heating discussed here would reduce the luminosity of the haloes filling the entire void volume rendering those galaxies even more difficult to detect.

The HOD used by Tinker and Conroy implies that the mass-to-light ratio increases by a factor of ten from haloes with a mass of  $10^{13} h^{-1} M_\odot$  to haloes with  $10^{10} h^{-1} M_\odot$ , independent of the environment. This is consistent with the compilation of the baryon content of galaxies by McGaugh [42]. Haloes with the mass of  $10^{10} h^{-1} M_\odot$  seem to host only 5% of the baryonic mass corresponding to the cosmic mean. In our simulations we do not find any indication that the UV-background reduces the baryon fraction in galaxies significantly more massive than the characteristic mass. Therefore, we speculate that stellar feedback plays a key role in reducing the baryon fraction galaxies with  $M_{\text{tot}} > M_{1/2}$ . Note that the baryon fractions in Ref. [42] shows indeed a break at  $v_{\text{circ}} \approx 30 \text{ km s}^{-1}$ , consistent with our findings for the characteristic mass.

In summary, the surprising low number of low-luminosity galaxies in voids can be explained by a mass-dependent mass-to-light ratio, as obtained from a global Halo Occupation Distribution and from a

proper mass modelling of galaxies. Haloes above the characteristic mass are expected to reside close to the walls of voids. The photo-heating discussed here reduces the luminosity of the low-mass and low-luminosity galaxies which can populate the entire void volume. Current surveys are limited to detect galaxies close to the walls due to the sensitivity limits of the surveys.

## 4 Why small haloes fail to accrete gas

In the previous section we have shown that dark matter haloes with  $v_{\text{max}} \ll 40 \text{ km s}^{-1}$  do accrete dark matter for  $z \lesssim 4$  while they do not accrete baryons for smaller redshifts. Halos with  $v_{\text{max}} < 35 \text{ km s}^{-1}$  are generally baryon deficient for  $z = 0$ . These results are obtained for high-resolution hydrodynamical cosmological simulations including a homogeneous photo-heating of an optically thin medium and including radiative cooling for a primordial chemical composition. In this section we investigate in detail the origin of the baryon deficiency which is evidently related to the photo-heating by the UV background. To this end we set up an analytic model and investigate how baryons cool in dwarf galaxies.

### 4.1 Outline of the analytic model

Our simple model is constructed as follows: In the beginning the gas in the universe is homogeneously distributed. In the process of structure formation gas is accreted by galaxies, i.e. its density increases.

Starting from a homogenous distribution the gas in the periphery of haloes and in the IGM follows the evolution of the dark matter. For our model here we assume that there is universal evolution of the overdensity,  $\Delta(t, \Delta_0)$ , which only depends on the time and on the final overdensity, see Fig. 4. By the help of Eq.(1) we can determine the temperature as a function of the overdensity. For a given temperature-density relation we can determine the gas density profile of NFW-type haloes. Assuming that the gas density in the periphery of the halo is given by the mean cosmic baryon fraction we can

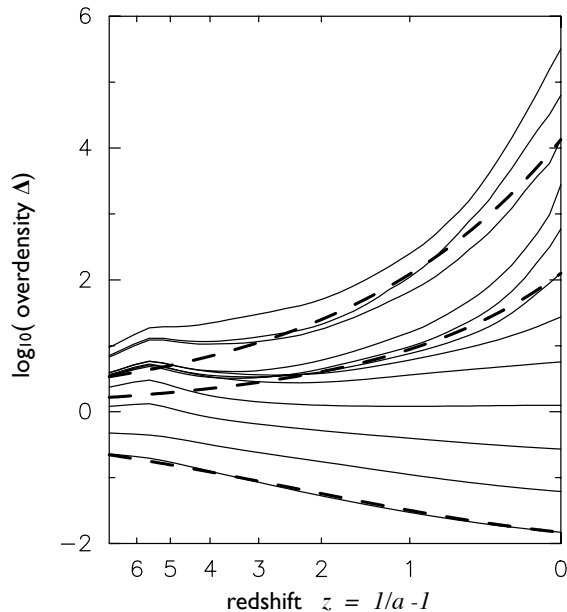


**Figure 4:** The overdensity evolution  $\Delta(a, \Delta_0)$ . We group in the simulation snapshot for  $z = 0$  all particles according to their overdensity. Then trace back the density of the SPH-particles and compute the average density of the groups for earlier redshifts (solid lines). Moreover, we show three approximated overdensity evolutions (dashed lines) according to Eq. (4). See Sec. 4.2 for details. The peak-like structures at  $z \approx 6$  are caused by photo-evaporation and are neglected in our approximation.

determine the central gas density and temperature. If the resulting cooling time is short the halo would accrete baryonic matter, if the cooling time is long the halo would fail to accrete baryonic matter.

## 4.2 Effective equation of state of the IGM

For a known overdensity evolution,  $\Delta(t, \Delta_0)$ , we can integrate the thermal evolution of the IGM, Eq. (1). To determine the heating and the cooling,  $\mathcal{H}(t)$  and  $\Gamma(t)$ , respectively, we have to know the abundance of each species, i.e. the ionisation state of hydrogen and helium. As in the cosmological

simulations we adopt collisional equilibrium, hence, we can determine for a given time and a given temperature the relative abundances. We solve the rate equations for collisional ionisation, for recombination, and for photo-ionisation. Now we can compute the photo-heating and cooling of the gas. Time-dependent specific energy injection rates,  $\epsilon_i$ , are tabulated according to the UV-background model. As a result the total photo-heating can be written as  $\mathcal{H} = n_{\text{HI}}\epsilon_{\text{HI}} + n_{\text{HeI}}\epsilon_{\text{HeI}} + n_{\text{HeII}}\epsilon_{\text{HeII}}$ . Cooling rates are used as given in [29]. Hence, for a given overdensity evolution,  $\Delta(t, \Delta_0)$  and UV-background model we can compute the final gas temperature,  $T(t_0, \Delta_0)$ .

We use our numerical simulations to estimate the overdensity evolution,  $\Delta(t, \Delta_0)$ . In Gadget the hydrodynamical equations are solved by the SPH method, hence, the fluid is represented by mass elements. The SPH-particles can be traced through the simulation. We group SPH-particles according to their overdensity at the end of the simulation,  $\Delta_0$ , regardless if they are located in a galaxy, in a cosmological filament or in the field. Then, we trace back the density of the particles and compute the average density of each group, see Fig. 4. For the integration of the thermal evolution of the IGM we approximate the overdensity evolution by an analytic expression, namely

$$\log \Delta(t, \Delta_0) = \log \Delta_0 \cdot \left| \frac{G(a, \Delta_0)}{G(1, \Delta_0)} \right|, \quad (4)$$

where we use the cosmic expansion factor,  $a = 1/(z + 1)$ , as time variable. We approximate the time evolution by  $G(a, \Delta_0) = |(a + 1)^{m(\log \Delta_0)} - 1|$ , and determine for each final overdensity the exponent  $m(\log \Delta_0)$ . We fit Eq. (4) to each curve in Fig. 4, where we take only the data for  $z \leq 3$  into account. In the overdensity range  $-2 < \log \Delta_0 < 6$  the resulting exponents are reasonably reproduced by  $m(\log \Delta_0) = 1.3 \log \Delta_0 - 0.26 (\log \Delta_0)^2$ . This finally provides an analytic model for the overdensity evolution,  $\Delta(t, \Delta_0)$ .

In Fig. 5 the temperature-density relation,  $T(\Delta, t_0)$ , obtained by integrating Eq. (1) using

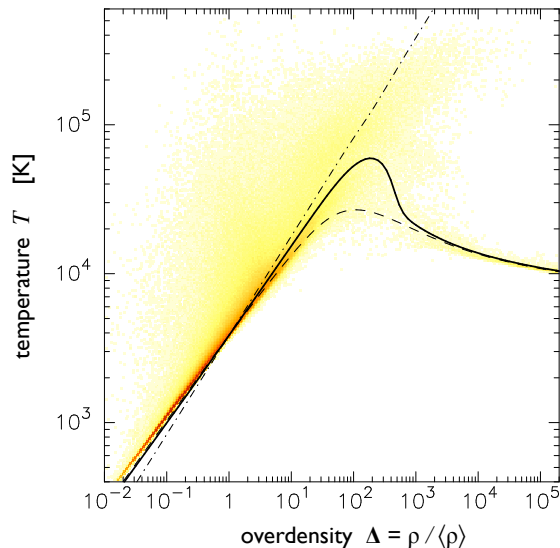


**Figure 5:** Temperature-density relation,  $T(\Delta, t_0)$  for the overdensity histories as given in Eq. (4) (thick solid line). In addition two extreme scenarios for the overdensity history are shown. First, all gas is compressed or decompressed to its final overdensity,  $\Delta_0$ , at the very beginning, i. e. before reionisation takes place (dashed-dotted line). Secondly, all gas evolves at cosmic mean density until  $z = 0$  and is then instantaneously compressed or decompressed to its final overdensity. The latter clearly results in an adiabatic relation (dash-dotted line). Finally, the distribution of the SPH-particles in the simulation is shown.

the analytic formula for the overdensity evolution described above, is shown. For comparison the density-temperature phase-space, as obtained from the numerical simulation, is also depicted. For high densities,  $\Delta \gtrsim 10^3$ , the analytic result,  $T(\Delta, t_0)$ , and the distribution of the SPH-particle coincides very well, because the thermal state is determined by thermal equilibrium. For low densities, most of the SPH-particles also follow  $T(\Delta, t_0)$ . Finally, a significant fraction of the SPH-particles has temperatures substantially above  $T(\Delta, t_0)$ , since in the numerical simulation particles are also heated by dissipation at shock fronts.

Which impact has the overdensity evolution? To

answer this question we investigate two extreme scenarios. First, gas stays at mean cosmic density until  $z = 0$  and is then instantaneously compressed or decompressed to the final overdensity. This clearly leads to an adiabatic temperature-density relation, see Fig. 5 (dash-dotted line). Secondly, gas is brought to the final overdensity before reionisation takes place and has then constant overdensity. The resulting temperature-density (dashed line) relation is only slightly different from the result for the average cosmic density evolution (solid line); the transition to thermal balance occurs at lower overdensities, since the compressed gas has more time to cool.

For the overdensity history introduced in Eq. (4) we find for low overdensities,  $\Delta \lesssim 100$ , an effective equation-of-state, i. e. the temperature-density relation follows a power-law,

$$T_{\text{eos}}(\Delta, t = t_0) = T_0 \Delta^\alpha, \quad (5)$$

with  $T_0 = 3.85 \times 10^3$  K and  $\alpha = 0.59$ .

By plotting the cooling times in the temperature-density phase-space we can clearly see at which overdensities the gas is in thermal balance, see Fig. 6. For low overdensities,  $\Delta \lesssim 10^2$ , cooling has only a negligible effect, i. e. the thermal state of the gas is determined by the cumulative photo-heating. In contrast, at high overdensities,  $\Delta \gtrsim 10^3$ , the temperature lies exactly at the boundary between heating and cooling, i. e. it is in thermal balance. Therefore, in the range  $10^2 < \Delta < 10^3$  the transition from the pure photo-heating to the equilibrium between heating and cooling takes place.

### 4.3 The halo density profile

We now set up the second part of our toy model, namely, the spherical halo model, with the aim to estimate the innermost gas density as a function of halo mass.

For a spherically symmetric halo in hydrostatic equilibrium the pressure force and the gravitational

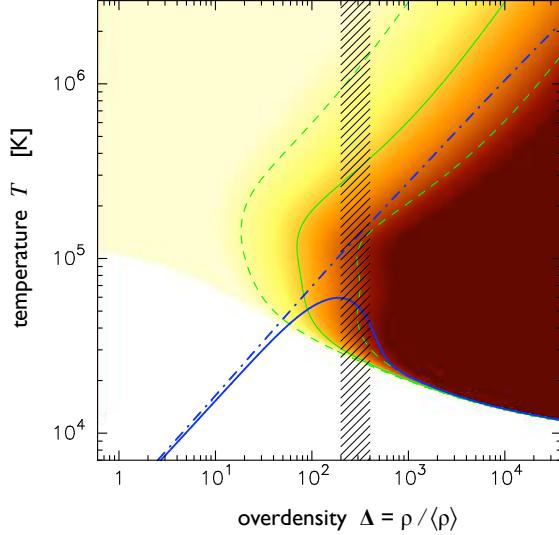


**Figure 6:** Theoretical result for  $T(\Delta)$  with cooling (solid line) and without (dash-dotted line). The result without cooling follows the power-law  $T = 3.85 \text{ K } (\delta + 1)^{0.595}$ . Cooling times are indicated by colours and contour lines. Contours from left to right are at 10x Hubble time (dashed line), Hubble time (solid line), and 0.1x Hubble time (dash-dotted line). Cooling times are also indicated by colours, the blank area indicate the regime of UV heating. The hashed area highlights the transition region from cumulative photo-heating to thermal balance.

force are in balance,

$$\frac{1}{\rho} \frac{dP}{dr} = -\frac{GM_{\text{tot}}(< r)}{r^2}, \quad (6)$$

where  $G$  is the gravitational constant and  $M_{\text{tot}}(< r)$  is the total mass enclosed by the radius  $r$ . Assuming an effective equation-of-state, as given in Eq. (5), we can write the left-hand side of Eq. (6) in terms of the gas overdensity. To this end we expand the gas density,  $\rho = \Delta n_b m_p$ , where  $m_p$  is the proton mass. The pressure can be written as  $P = \Sigma_i n_i k_B T = (\Delta n_b / \mu) k_B T_0 \Delta^\alpha$ , where we have used the molecular weight,  $\mu = n_b / \Sigma_i n_i$ , and Eq. (5). Now we rewrite the left-hand side of Eq. (6),

$$\frac{k_B T_0}{\mu m_p} (\alpha + 1) \Delta^{\alpha-1} \frac{d\Delta}{dr}. \quad (7)$$

We simplify the right-hand side of Eq. (6) by assuming that the distribution of the total mass is determined by the dark matter. For the density profile of the latter we follow Ref. [45],

$$\rho_{\text{dm}} = \rho_s \frac{4}{x(1+x)^2}, \quad (8)$$

with  $x = r/r_s$ . The scaling radius,  $r_s$ , is related to the virial radius,  $r_{\text{vir}}$ , of a halo by  $r_s = r_{\text{vir}}/c$ , where  $c$  is the concentration parameter. The mass enclosed by the scaled radius  $x$  is

$$\begin{aligned} M(< x) &= 16\pi r_s^3 \rho_s \left\{ \ln(1+x) - \frac{x}{1+x} \right\} \\ &= 16\pi r_s^3 \rho_s F(x). \end{aligned} \quad (9)$$

Evidently, the virial radius encloses the virial mass,  $M_{\text{vir}} = M(< c)$ . Dividing Eq. (9) by the virial mass leads to

$$M(< x) = M_{\text{vir}} F(x)/F(c). \quad (10)$$

Using  $r = r_{\text{vir}}x/c$  and the expression Eq. (7) we can rewrite Eq. (6)

$$\frac{k_B T_0}{\mu m_p} (\alpha + 1) \Delta^{\alpha-1} d\Delta = \frac{GM_{\text{vir}}}{r_{\text{vir}}} \frac{F(x)}{F(c)} \frac{c}{x^2} dx. \quad (11)$$

We can further simplify the expression on the right-hand side by introducing the maximum circular velocity. The circular velocity is given by

$$\begin{aligned} v_{\text{circ}}(r) &= \sqrt{\frac{GM(< r)}{r}} \\ &= \sqrt{\frac{GM_{\text{vir}} c}{r_{\text{vir}} x} \frac{F(x)}{F(c)}}. \end{aligned} \quad (12)$$

The quotient  $F(x)/x$  is independent from the halo properties and has a maximum value of  $\sim 0.22$ . Therefore, we can write for the maximum circular velocity

$$v_{\text{max}}^2 = \frac{GM_{\text{vir}}}{r_{\text{vir}}} \frac{0.22 c}{F(c)}. \quad (13)$$

Eq. (11) is now independent from the concentration parameter of the halo, namely

$$\frac{k_B T_0}{\mu m_p} (\alpha + 1) \Delta^{\alpha-1} d\Delta = \frac{v_{\text{max}}^2}{0.22} \frac{F(x)}{x^2} dx. \quad (14)$$

To determine the innermost gas overdensity we integrate Eq. (14) starting from the periphery of the halo,  $x = x_{\text{out}}$ , to the center,  $x = 0$ . Since the halo gas is highly ionised we adopt  $\mu = 0.59$ . The resulting central overdensity is

$$\Delta_{\text{centre}}^{\alpha} = \left( \frac{T_0}{10^4 \text{ K}} \right)^{-1} \left( \frac{v_{\text{max}}}{5.6 \text{ km s}^{-1}} \right)^2 \times \frac{\alpha}{(\alpha + 1)} \left( 1 - \frac{\ln(1 + x_{\text{out}})}{x_{\text{out}}} \right) + \Delta_{\text{out}}^{\alpha}, \quad (15)$$

where  $\Delta_{\text{out}}$  is the gas overdensity at  $x_{\text{out}}$ . We estimate the outer overdensity by assuming that it is identical to the dark matter overdensity.

From Eq. (8) we get

$$\Delta_{\text{dm}} = \frac{\rho_{\text{dm}}}{\langle \rho_{\text{dm}} \rangle} = \frac{\rho_{\text{s}}}{\langle \rho_{\text{dm}} \rangle} \frac{4}{x(1+x)^2}. \quad (16)$$

The virial radius is determined by the cumulative overdensity,  $\Delta_{\text{c}}(z)$ , at which virialisation is expected. We use the approximation of Ref. [3] for  $\Delta_{\text{c}}(z)$ . For the virial mass we write now

$$M_{\text{vir}} = \frac{4}{3} \pi r_{\text{vir}}^3 \Delta_{\text{c}} \langle \rho_{\text{dm}} \rangle = 16 \pi r_{\text{s}}^3 \rho_{\text{s}} F(c), \quad (17)$$

where we have used Eq. (9) for the last equality. Substituting  $r_{\text{s}}/\langle \rho_{\text{dm}} \rangle$  we can write for Eq. (16)

$$\Delta_{\text{dm}}(x_{\text{out}}) = \frac{\Delta_{\text{c}}(z)}{3} \frac{c^3}{F(c)} \frac{1}{x_{\text{out}}(1+x_{\text{out}})^2}, \quad (18)$$

which allows us to estimate  $\Delta_{\text{out}}$  in Eq. (15).

We wish to give the central gas overdensity as a function of the maximum circular velocity. To utilise Eq. (18) we have to find a relation between  $v_{\text{max}}$  and the concentration parameter. Maccio *et al.* [39] give an relation between  $c$  and the virial mass of a halo for  $z = 0$ ,

$$c(M_{\text{vir}}) = 10.47 \times \left( \frac{M_{\text{vir}}}{10^{12} h^{-1} M_{\odot}} \right)^{-0.109}. \quad (19)$$

From our simulations we find that  $M_{\text{vir}}$  and the maximum circular velocity are on average related by

$$\frac{M_{\text{vir}}}{10^{12} h^{-1} M_{\odot}} = \left( \frac{v_{\text{max}}}{210 \text{ km s}^{-1}} \right)^{2.9}. \quad (20)$$

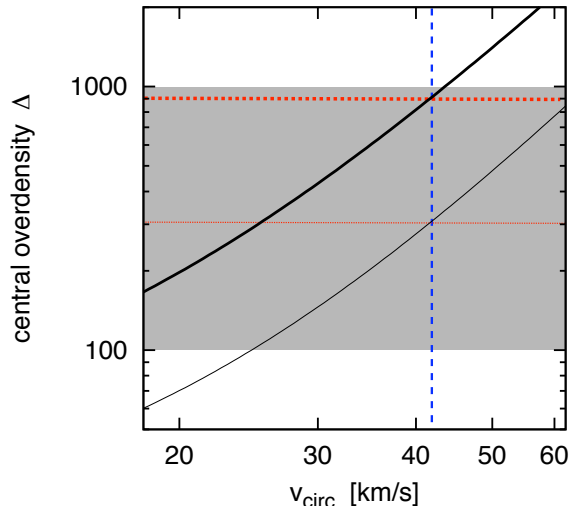


**Figure 7:** Central gas overdensity as a function of the halo circular velocity. We compute the central overdensity according to Eq. (15) (thick solid line). Moreover, we plot the overdensity at the scaling radius,  $r_{\text{s}}$  (thin solid line). The grey area indicates the transition region from pure UV heating to thermal balance, see Sec. 4.2 or Fig. 6. The blue dashed line indicates the characteristic circular velocity obtained from the numerical simulations. The thick and the thin red dotted lines indicate a condensation criterion of  $\Delta = 900$  and  $300$ , respectively.

Moreover, the concentration parameter is expected to scale with redshift according to  $c \sim (1+z)^{-1}$  [69, 73]. Thus, we obtain an relation between concentration parameter and  $v_{\text{max}}$ , namely

$$c(v_{\text{max}}) = 10.47 \left( \frac{v_{\text{max}}}{210 \text{ km s}^{-1}} \right)^{-0.32} \frac{1}{(z+1)}, \quad (21)$$

which allows us finally to evaluate Eq. (15).

Finally, we compute the central gas overdensity as follows: For a given circular velocity we determine the concentration parameter of the halo by Eq. (21). Then we estimate the outer gas density, here we assume that  $\Delta(x_{\text{out}}) = \Delta_{\text{dm}}(x_{\text{out}})$ , see Eq. (18), at three times the virial radius,  $x_{\text{out}} = 3c$ . Finally, we compute the central gas overdensity, Eq. (15), as a function of the circular velocity, see Fig. 7.

To estimate the characteristic circular velocity by our analytic model we have to give a criterion at which central overdensity gas condenses in a halo centre. The transition from the effective equation-of-state to the thermal balance takes place in the overdensity range of  $10^2 < \Delta < 10^3$ . For an overdensity of 900 our analytic model would match the characteristic circular velocity obtained from the numerical simulations. However, the resolution in the numerical simulation is not sufficient to reach the innermost gas density as assumed in our model. To mimic the numerical resolution we integrate Eq. (15) only up to the scaling radius, see thin line in Fig. 7. In this case an overdensity of 300 corresponds to the characteristic circular velocity. This leads to two conclusions: First, the analytic model matches the numerical result very well. Secondly, better resolved simulations may result in a lower characteristic velocity. However, gas mixing in the halo centre may generally prohibit an ideal hydrostatic equilibrium.

#### 4.4 Evolution of the characteristic mass

In the previous section we have shown that our model well reproduces the characteristic circular velocity at  $z = 0$ . We can easily extend the model to other redshifts by determining the effective e.o.s and the criterion for condensation as a function of redshift. We derive the time-dependent e.o.s. by integrating Eq. (1), see Sec. 4.2. To obtain a time-dependent condensation criterion we determine the position of the maximum in the density-temperature relation, see the solid line in Fig. 5. To compensate for the discrepancy between  $\Delta_{\max}$  and the actual overdensity for condensation we introduce a correction factor. To match the characteristic circular velocity obtained from the simulations this factor also comprises the effect of the limited numerical resolution. Eq. (15) can be now rewritten

$$\left(\frac{v_{1/2}}{5.6 \text{ km s}^{-1}}\right)^2 = \Delta_{\max}^{\alpha} f_{\text{corr}} \frac{T_0}{10^4 \text{ K}} \frac{\alpha + 1}{\alpha}, \quad (22)$$

where we have neglected the contribution of the outer halo boundary. To match the characteristic

circular velocity at  $z = 0$  we choose  $f_{\text{corr}} = 2.5$ . Eq. (22) indicates that the characteristic circular velocity is essentially determined by the density-temperature relation at any time. All parameters on the r.h.s., namely slope and normalisation of the e.o.s. and  $\Delta_{\max}$ , are derived from  $T(\Delta, t)$ . Fig. 8 (upper row) shows how the characteristic circular velocity is composed of three parameters of the temperature-density relation. The upper left panel shows  $T(\Delta)$  for several redshifts. The next three panels show the evolution of the parameters of  $T(\Delta, t)$ : The temperature  $T_0$ , the overdensity at the maximal temperature,  $\Delta_{\max}$ , and the slope  $d \log T(\Delta, t) / d \log \Delta$  at  $\Delta = 1$ . The right panel shows the resulting  $v_{1/2}$ , which nicely matches the characteristic circular velocity obtained from the numerical simulations. In the range  $3 \gtrsim z \geq 0$  the circular velocity is virtually constant. This is the result of the decreasing  $T_0$  and the increasing  $\Delta_{\max}$ .

The redshift evolution of the characteristic mass can be derived from characteristic circular and Eq. (13) and Eq. (17). Combining these equations and using  $\langle \rho \rangle \propto (z + 1)^3$  we find

$$M_{1/2} \propto v_{1/2}^3 \Delta_c^{-1/2} (z) (z + 1)^{-3/2}. \quad (23)$$

This is in agreement with the results found earlier [22]. More precisely, the dominating terms in  $M_{1/2}$  are introduced by the redshift dependence in the definition of the virial radius, Eq. (17).

#### 4.5 Variations in the UV background

As shown above the cumulative heating of the IGM by the UV background prevents the gas cooling in the centre of small mass haloes. It is therefore evident that the characteristic mass depends on the UV background and its evolution over cosmic times. We use our model worked out above to assess the impact of modifications of the UV background model on the characteristic circular velocity. We first consider changes of the UV flux density and secondly of the UV spectrum.

**UV flux density** The flux density of the UV background has only a small effect on the temperature of



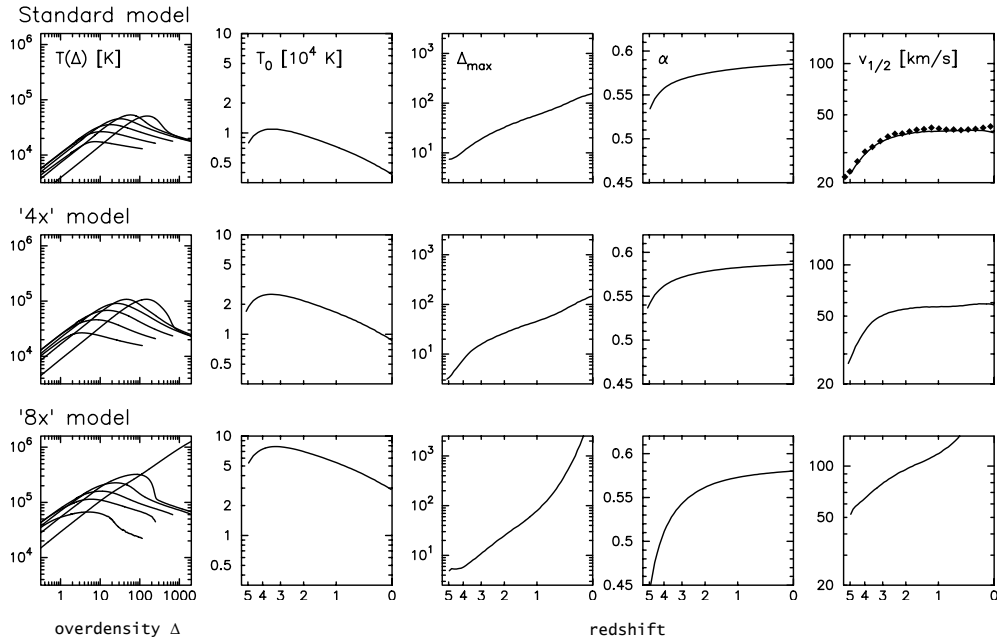


**Figure 8:** *Left panels:* The density-temperature  $T(\Delta, t)$  for several redshifts and three different UV-background models. The next three columns show the redshift evolution of the parameters of  $T(\Delta, t)$ : The normalisation and the effective e.o.s.,  $T_0$ , the position of the maximum,  $\Delta_{\max}$ , and the slope of the e.o.s.,  $\alpha$ . Finally, for each UV-background model the resulting characteristic circular velocity is shown, see Eq. (22). The upper right panel shows also the characteristic velocity obtained from the numerical simulations.

the IGM. The reason is that a higher flux reduces the fraction of neutral hydrogen in the tenuous IGM, hence, the higher flux finds fewer neutral atoms to ionise. As a result the heating rate is essentially independent from the flux density, when photo-ionisation dominates over collisional ionisation and as long as the spectrum remains unchanged. In this case the fraction of neutral hydrogen,  $x_{\text{HI}} = 1 - x_{\text{HII}}$ , can be derived from the balance between photo-ionisation and recombination

$$\Gamma_{\gamma\text{HI}} x_{\text{HI}} n_{\text{H}} = \alpha_{\text{HII}}(T) x_{\text{HII}} n_{\text{H}} n_{\text{e}}. \quad (24)$$

The IGM is generally highly ionised, hence  $x_{\text{HII}} \sim 1$ . In this case the electron density is proportional to the hydrogen density,  $n_{\text{e}} \sim n_{\text{H}}$ . As a result the heating due to hydrogen ionisation becomes

$$\mathcal{H}_{\text{HI}} = n_{\text{HI}} \epsilon_{\text{HI}} \sim \alpha_{\text{HII}}(T) \frac{\epsilon_{\text{HII}}}{\Gamma_{\gamma\text{HI}}} n_{\text{H}}^2. \quad (25)$$

The heating therefore depends only on the ratio  $\epsilon_{\text{HII}}/\Gamma_{\gamma\text{HI}}$ , i.e. only on the average energy input per ionisation event. In the limits made above the heat input is independent from the actual flux density. In accordance with this result we have found in Ref. [22] that the characteristic mass depends only little on the UV background flux density. Even very strong variations of the flux causes only a small shift of the characteristic mass, showing that the latter is sensitive only to the thermal state of the IGM which is little affected by the actual flux density.

**UV spectrum** Significantly more important for the thermal evolution of the IGM is the spectrum of the UV background. As a first guess one may expect that the final temperature of the IGM is directly proportional to the energy per ionising photon. However, since the recombination rate,  $\alpha_{\text{HII}}(T)$ , decreases with increasing temperature the effect is

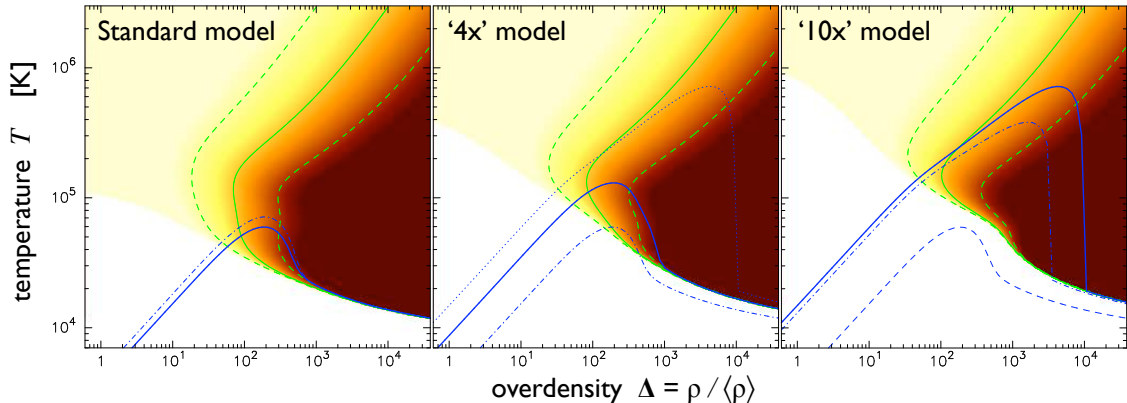


**Figure 9:** Theoretical results for temperature distribution in the IGM as a result of different UVB heating models. *Left panel:* The thick solid line indicate the result for our standard model according to [20]. Color coded is the cooling time. The blank area indicates the region where the gas is heated. Three contour lines are shown, they indicate from the left to right a cooling time 10x, 1x, and 0.1x the Hubble time. The dashed blue line indicates a four times increased energy per ionising photon only for  $z > 2$ . *Middle panel:* Results for four times increased energy per ionising photon for all redshifts. For comparison the dashed blue line indicates temperature distribution resulting from the standard model as shown in the left panel. *Right panel:* Results for ten times increased energy per ionising photon for all redshifts. For comparison also the eight times increased energy and the standard heating as shown in the left panel are indicated.

not that strong. Fig. 9 shows the results for increased energies per ionising photon compared to the [20] model. We have computed models with four times and with eight times increased energy per ionisation event. The higher average energy shifts the effective equation-of-state to higher temperatures. Also the shape of the temperature-density relation changes. The maximum in the relation shifts to higher densities. In particular, the maximum changes significantly between the four times and eight times increased model. The effective equation-of-state runs in the cooling regime virtually parallel to lines of constant cooling times. When  $T_0 \gtrsim 1.5 \times 10^4$  K these cooling times are above the Hubble time. In those cases the transition to thermal balance appears at very high overdensities.

We use the models introduced above to estimate the impact of the UV spectrum on the characteristic circular velocity. To this end we compute the evolution of the characteristics of the temperature-density relation, see Fig. 8. For the four times increased energy per ionising photon we find that the characteris-

tic circular velocity amounts to  $\sim 60 \text{ km s}^{-1}$  for  $z \lesssim 2$ . For the eight times increased model the characteristic velocity get very high, since  $\Delta_{\text{max}}$  shifts to very high overdensities.

## 5 Summary

We discuss high-resolution simulations including radiative cooling and photo-heating. We focus on the baryon content of dwarf galaxy-sized dark matter haloes. To this end, we have simulated the structure formation in two distinct cosmological environments and we found that the characteristic mass below which haloes are baryon deficient does not depend on the environment. Moreover, we found that in haloes in the mass range of  $\sim 10^9$  to  $10^{10} h^{-1} M_{\odot}$  in general gas condensation stops at some redshift between reionisation and today. In our simulation those haloes are able to retain the already condensed gas, allowing further star formation. We have derived the characteristic mass in newly accreted matter, which is somewhat higher than the characteristic mass of

the baryon fraction in the haloes. The former is more appropriate for semi-analytic modelling.

Tinker and Conroy [64] found by a Halo Occupation Distribution analysis that the magnitude of galaxies which reside in haloes with a mass about the characteristic mass is  $M_r \sim -10$ . Moreover, they found that more luminous void galaxies, i.e.  $M_r > -10$ , are preferably located close to the walls of the voids. Therefore, photo-heating would reduce the baryon content of the small-mass haloes populating the entire void volume, rendering these galaxies even more dark. Current surveys which cover large void volumes are not sensitive enough to detect the galaxies affected by photo-heating.

The failure of condensing gas can be traced back to the cooling time in the halo centre, which may exceed the Hubble time. We have set up a spherical model for the haloes gas density profile. Crucial for this model is the effective equation of state which we have derived by integrating the thermal history of the IGM using an approximation for the overdensity evolution as a function of the final overdensity. We have justified this model by considering the density contrast evolution in the simulation. This spherical model allows us to derive the characteristic mass for different heating histories of the IGM.

We find that the mass at which galaxy formation seems to fade can be explained by a heating model which incorporates 6-8 times more energy per ionising photon than given in the Haardt & Madau model [20]. For redshift  $z \gtrsim 3$  it is known from analyses of the Lyman $\alpha$  forest that the temperature of the IGM is higher than obtained by a naive application of the Haardt & Madau model. The derived temperature implies a 3-4 times increased energy per ionising photon, or a more efficient heating due to non-equilibrium effects or radiative transfer effects. We found that if the average temperature of the IGM is today as high as  $\gtrsim 10^4$  K dwarf galaxy formation would be suppressed at a mass scale consistent with that derived, e.g., by the conditional luminosity function. Therefore, the mass scale for suppression of dwarf galaxy formation may

be considered as a measure for the temperature of gas in the surroundings of dwarf galaxies. The heat source could be the UV background or alternatively any feedback of the galaxy.

**Acknowledgement:** The simulations discussed here have been performed at the LRZ Munich and the NIC Jülich. We would like to thank Gustavo Yepes and Volker Springel for many comments and discussions during the last years. Finally, we would like to thank our referees, in particular Michael Vogelely, who read the paper very carefully and provided many comments which improved this text.

## References

- [1] A. J. Benson, C. S. Frenk, C. G. Lacey, C. M. Baugh, and S. Cole. The effects of photoionization on galaxy formation - II. Satellite galaxies in the Local Group. *MNRAS*, 333:177–190, June 2002.
- [2] J. R. Bond, S. Cole, G. Efstathiou, and N. Kaiser. Excursion set mass functions for hierarchical Gaussian fluctuations. *ApJ*, 379:440–460, October 1991.
- [3] G. L. Bryan and M. L. Norman. Statistical Properties of X-Ray Clusters: Analytic and Numerical Comparisons. *ApJ*, 495:80–+, March 1998.
- [4] L. Ceccarelli, N. D. Padilla, C. Valotto, and D. G. Lambas. Voids in the 2dFGRS and  $\Lambda$ CDM simulations: spatial and dynamical properties. *MNRAS*, 373:1440–1450, December 2006.
- [5] J. M. Colberg, F. Pearce, C. Foster, E. Platen, R. Brunino, M. Neyrinck, S. Basilakos, A. Fairall, H. Feldman, S. Gottlöber, O. Hahn, F. Hoyle, V. Müller, L. Nelson, M. Plienis, C. Porciani, S. Shandarin, M. S. Vogelely, and R. van de Weygaert. The Aspen-Amsterdam void finder comparison project. *MNRAS*, 387:933–944, June 2008.

- [6] D. J. Croton, E. Gaztañaga, C. M. Baugh, P. Norberg, M. Colless, I. K. Baldry, J. Bland-Hawthorn, T. Bridges, R. Cannon, S. Cole, C. Collins, W. Couch, G. Dalton, R. De Propris, S. P. Driver, G. Efstathiou, R. S. Ellis, C. S. Frenk, K. Glazebrook, C. Jackson, O. Lahav, I. Lewis, S. Lumsden, S. Maddox, D. Madgwick, J. A. Peacock, B. A. Peterson, W. Sutherland, and K. Taylor. The 2dF Galaxy Redshift Survey: higher-order galaxy correlation functions. *MNRAS*, 352:1232–1244, August 2004.
- [7] J. Einasto, M. Einasto, and M. Gramann. Structure and formation of superclusters. IX - Self-similarity of voids. *MNRAS*, 238:155–177, May 1989.
- [8] J. Einasto, M. Einasto, M. Gramann, and E. Saar. Structure and formation of superclusters. XIII - The void probability function. *MNRAS*, 248:593–605, February 1991.
- [9] H. El-Ad and T. Piran. Voids in the Large-Scale Structure. *ApJ*, 491:421–+, December 1997.
- [10] H. El-Ad and T. Piran. A case devoid of bias: Optical Redshift Survey voids versus IRAS voids. *MNRAS*, 313:553–558, April 2000.
- [11] O. Fakhouri and C.-P. Ma. Dark matter halo growth - II. Diffuse accretion and its environmental dependence. *MNRAS*, pages 1746–+, November 2009.
- [12] Y. Friedmann and T. Piran. A Model of Void Formation. *ApJ*, 548:1–6, February 2001.
- [13] S. R. Furlanetto and T. Piran. The evidence of absence: galaxy voids in the excursion set formalism. *MNRAS*, 366:467–479, February 2006.
- [14] S. Ghigna, S. A. Bonometto, J. Retzlaff, S. Gottloeber, and G. Murante. Void Analysis as a Test for Dark Matter Composition? *ApJ*, 469:40–+, September 1996.
- [15] S. Ghigna, S. Borgani, S. A. Bonometto, L. Guzzo, A. Klypin, J. R. Primack, R. Giovanelli, and M. P. Haynes. Sizes of voids as a test for dark matter models. *ApJL*, 437:L71–L74, December 1994.
- [16] D. M. Goldberg, T. D. Jones, F. Hoyle, R. R. Rojas, M. S. Vogeley, and M. R. Blanton. The Mass Function of Void Galaxies in the Sloan Digital Sky Survey Data Release 2. *ApJ*, 621:643–650, March 2005.
- [17] S. Gottlöber, E. L. Lokas, A. Klypin, and Y. Hoffman. The structure of voids. *MNRAS*, 344:715–724, September 2003.
- [18] S. A. Gregory and L. A. Thompson. The Coma/A1367 supercluster and its environs. *ApJ*, 222:784–799, June 1978.
- [19] N. A. Grogin and M. J. Geller. An Imaging and Spectroscopic Survey of Galaxies within Prominent Nearby Voids. I. The Sample and Luminosity Distribution. *AJ*, 118:2561–2580, December 1999.
- [20] F. Haardt and P. Madau. Radiative Transfer in a Clumpy Universe. II. The Ultraviolet Extragalactic Background. *ApJ*, 461:20–+, April 1996.
- [21] G. Hinshaw, J. L. Weiland, R. S. Hill, N. Odegard, D. Larson, C. L. Bennett, J. Dunkley, B. Gold, M. R. Greason, N. Jarosik, E. Komatsu, M. R.olta, L. Page, D. N. Spergel, E. Wollack, M. Halpern, A. Kogut, M. Limon, S. S. Meyer, G. S. Tucker, and E. L. Wright. Five-Year Wilkinson Microwave Anisotropy Probe Observations: Data Processing, Sky Maps, and Basic Results. *ApJS*, 180:225–245, February 2009.
- [22] M. Hoeft, G. Yepes, S. Gottlöber, and V. Springel. Dwarf galaxies in voids: suppressing star formation with photoheating. *MNRAS*, 371:401–414, September 2006.
- [23] Y. Hoffman and J. Shaham. On the origin of the voids in the galaxy distribution. *ApJL*, 262:L23–L26, November 1982.
- [24] F. Hoyle, R. R. Rojas, M. S. Vogeley, and J. Brinkmann. The Luminosity Function of Void

- Galaxies in the Sloan Digital Sky Survey. *ApJ*, 620:618–628, February 2005.
- [25] F. Hoyle and M. S. Vogeley. Voids in the Point Source Catalogue Survey and the Updated Zwicky Catalog. *ApJ*, 566:641–651, February 2002.
- [26] F. Hoyle and M. S. Vogeley. Voids in the Two-Degree Field Galaxy Redshift Survey. *ApJ*, 607:751–764, June 2004.
- [27] A. Jenkins, C. S. Frenk, S. D. M. White, J. M. Colberg, S. Cole, A. E. Evrard, H. M. P. Couchman, and N. Yoshida. The mass function of dark matter haloes. *MNRAS*, 321:372–384, February 2001.
- [28] M. Joeveer, J. Einasto, and E. Tago. Spatial distribution of galaxies and of clusters of galaxies in the southern galactic hemisphere. *MNRAS*, 185:357–370, November 1978.
- [29] N. Katz, D. H. Weinberg, and L. Hernquist. Cosmological Simulations with TreeSPH. *ApJS*, 105:19–+, July 1996.
- [30] R. P. Kirshner, A. Oemler, P. L. Schechter, and S. A. Shectman. A million cubic megaparsec void in Bootes. *ApJL*, 248:L57–L60, September 1981.
- [31] A. Klypin, S. Gottlöber, A. V. Kravtsov, and A. M. Khokhlov. Galaxies in N-Body Simulations: Overcoming the Overmerging Problem. *ApJ*, 516:530–551, May 1999.
- [32] A. Klypin, A. V. Kravtsov, J. S. Bullock, and J. R. Primack. Resolving the Structure of Cold Dark Matter Halos. *ApJ*, 554:903–915, June 2001.
- [33] A. Klypin, A. V. Kravtsov, O. Valenzuela, and F. Prada. Where Are the Missing Galactic Satellites? *ApJ*, 522:82–92, September 1999.
- [34] S. E. Koysov, J. Yoo, H.-W. Rix, D. H. Weinberg, A. V. Macciò, and J. M. Escudé. A Quantitative Explanation of the Observed Population of Milky Way Satellite Galaxies. *ApJ*, 696:2179–2194, May 2009.
- [35] B. Kuhn, U. Hopp, and H. Elsaesser. Results of a search for faint galaxies in voids. *A&A*, 318:405–415, February 1997.
- [36] J. Lee and D. Park. Rotation of Cosmic Voids and Void Spin Statistics. *ApJ*, 652:1–5, November 2006.
- [37] Y.-S. Li, G. De Lucia, and A. Helmi. On the nature of the Milky Way satellites. *MNRAS*, pages 1727–+, November 2009.
- [38] U. Lindner, M. Einasto, J. Einasto, W. Freudling, K. Fricke, V. Lipovetsky, S. Pustilnik, Y. Izotov, and G. Richter. The distribution of galaxies in voids. *A&A*, 314:1–12, October 1996.
- [39] A. V. Macciò, A. A. Dutton, F. C. van den Bosch, B. Moore, D. Potter, and J. Stadel. Concentration, spin and shape of dark matter haloes: scatter and the dependence on mass and environment. *MNRAS*, 378:55–71, June 2007.
- [40] A. V. Maccio’, X. Kang, F. Fontanot, R. S. Somerville, S. E. Koysov, and P. Monaco. On the origin and properties of Ultrafaint Milky Way Satellites in a LCDM Universe. *ArXiv e-prints*, March 2009.
- [41] H. Mathis and S. D. M. White. *MNRAS*, 337:1193, 2002.
- [42] S. S. McGaugh, J. M. Schombert, W. J. G. de Blok, and M. J. Zagursky. The Baryon Content of Cosmic Structures. *ApJL*, 708:L14–L17, January 2010.
- [43] B. Moore, S. Ghigna, F. Governato, G. Lake, T. Quinn, J. Stadel, and P. Tozzi. Dark Matter Substructure within Galactic Halos. *ApJL*, 524:L19–L22, October 1999.
- [44] V. Müller, S. Arbabi-Bidgoli, J. Einasto, and D. Tucker. Voids in the Las Campanas Redshift Survey versus cold dark matter models. *MNRAS*, 318:280–288, October 2000.

- [45] J. F. Navarro, C. S. Frenk, and S. D. M. White. A Universal Density Profile from Hierarchical Clustering. *ApJ*, 490:493–+, December 1997.
- [46] T. Okamoto, L. Gao, and T. Theuns. Mass loss of galaxies due to an ultraviolet background. *MNRAS*, 390:920–928, November 2008.
- [47] S. G. Patiri, J. E. Betancort-Rijo, F. Prada, A. Klypin, and S. Gottlöber. Statistics of voids in the two-degree Field Galaxy Redshift Survey. *MNRAS*, 369:335–348, June 2006.
- [48] P. J. E. Peebles. Large-scale background temperature and mass fluctuations due to scale-invariant primeval perturbations. *ApJL*, 263:L1–L5, December 1982.
- [49] P. J. E. Peebles. The Void Phenomenon. *ApJ*, 557:495–504, August 2001.
- [50] M. Plionis and S. Basilakos. The size and shape of local voids. *MNRAS*, 330:399–404, February 2002.
- [51] C. C. Popescu, U. Hopp, and H. Elsaesser. Results of a search for emission-line galaxies towards nearby voids. The spatial distribution. *A&A*, 325:881–892, September 1997.
- [52] W. H. Press and P. Schechter. Formation of Galaxies and Clusters of Galaxies by Self-Similar Gravitational Condensation. *ApJ*, 187:425–438, February 1974.
- [53] R. R. Rojas, M. S. Vogeley, F. Hoyle, and J. Brinkmann. Photometric Properties of Void Galaxies in the Sloan Digital Sky Survey. *ApJ*, 617:50–63, December 2004.
- [54] V. Sahni, B. S. Sathyaprakah, and S. F. Shandarin. The evolution of voids in the adhesion approximation. *ApJ*, 431:20–40, August 1994.
- [55] S. Shandarin, H. A. Feldman, K. Heitmann, and S. Habib. Shapes and sizes of voids in the Lambda cold dark matter universe: excursion set approach. *MNRAS*, 367:1629–1640, April 2006.
- [56] R. K. Sheth and G. Tormen. Large-scale bias and the peak background split. *MNRAS*, 308:119–126, September 1999.
- [57] R. S. Somerville. Can photo-ionization quenching resolve the substructure crisis? *ApJ*, 572:L23–L26, June 2002.
- [58] V. Springel and L. Hernquist. Cosmological smoothed particle hydrodynamics simulations: the entropy equation. *MNRAS*, 333:649–664, July 2002.
- [59] V. Springel and L. Hernquist. Cosmological smoothed particle hydrodynamics simulations: a hybrid multiphase model for star formation. *MNRAS*, 339:289–311, February 2003.
- [60] V. Springel, N. Yoshida, and S. D. M. White. GADGET: a code for collisionless and gasdynamical cosmological simulations. *New Astronomy*, 6:79–117, April 2001.
- [61] A. V. Tikhonov, S. Gottlöber, G. Yepes, and Y. Hoffman. The sizes of minivoids in the local Universe: an argument in favour of a warm dark matter model? *MNRAS*, 399:1611–1621, November 2009.
- [62] A. V. Tikhonov and A. Klypin. The emptiness of voids: yet another overabundance problem for the  $\Lambda$  cold dark matter model. *MNRAS*, 395:1915–1924, June 2009.
- [63] J. Tinker, A. V. Kravtsov, A. Klypin, K. Abazajian, M. Warren, G. Yepes, S. Gottlöber, and D. E. Holz. Toward a Halo Mass Function for Precision Cosmology: The Limits of Universality. *ApJ*, 688:709–728, December 2008.
- [64] J. L. Tinker and C. Conroy. The Void Phenomenon Explained. *ApJ*, 691:633–639, January 2009.
- [65] F. C. van den Bosch, X. Yang, H. J. Mo, S. M. Weinmann, A. V. Macciò, S. More, M. Cacciato, R. Skibba, and X. Kang. Towards a concordant model of halo occupation statistics. *MNRAS*, 376:841–860, April 2007.

- [66] M. S. Vogeley, M. J. Geller, C. Park, and J. P. Huchra. Voids and constraints on nonlinear clustering of galaxies. *AJ*, 108:745–758, September 1994.
- [67] M. S. Vogeley, F. Hoyle, R. R. Rojas, and D. Goldberg. The Void Spectrum and Properties of Void Galaxies in the SDSS. In *Bulletin of the American Astronomical Society*, volume 36 of *Bulletin of the American Astronomical Society*, pages 1496–+, December 2004.
- [68] M. S. Warren, K. Abazajian, D. E. Holz, and L. Teodoro. Precision Determination of the Mass Function of Dark Matter Halos. *ApJ*, 646:881–885, August 2006.
- [69] R. H. Wechsler, J. S. Bullock, J. R. Primack, A. V. Kravtsov, and A. Dekel. Concentrations of Dark Halos from Their Assembly Histories. *ApJ*, 568:52–70, March 2002.
- [70] S. D. M. White and M. J. Rees. Core condensation in heavy halos - A two-stage theory for galaxy formation and clustering. *MNRAS*, 183:341–358, May 1978.
- [71] G. Yepes, R. Kates, A. Khokhlov, and A. Klypin. Hydrodynamical simulations of galaxy formation: effects of supernova feedback. *MNRAS*, 284:235–256, January 1997.
- [72] J. Zavala, Y. P. Jing, A. Faltenbacher, G. Yepes, Y. Hoffman, S. Gottlöber, and B. Catinella. The Velocity Function in the Local Environment from  $\Lambda$ CDM and  $\Lambda$ WDM Constrained Simulations. *ApJ*, 700:1779–1793, August 2009.
- [73] D. H. Zhao, Y. P. Jing, H. J. Mo, and G. Börner. Mass and Redshift Dependence of Dark Halo Structure. *ApJL*, 597:L9–L12, November 2003.